Postprint of: Szkodo M., Stanisławska A., Komarov A., Bolewski Ł., Effect of MAO coatings on cavitation erosion and tribological properties of 5056 and 7075 aluminum alloys, WEAR (2021), 203709, DOI: 10.1016/j.wear.2021.203709

Effect of MAO coatings on cavitation erosion and tribological properties of 5056 and 7075 aluminum alloys

Marek Szkodo [1,*], Alicja Stanisławska[1], Aleksandr Komarov [2] and Łukasz Bolewski [3]

[1] Gdańsk University of Technology, Mechanical Engineering Faculty, Gdansk, G. Narutowicza 11/12, 80-233 Gdańsk, Poland; mszkodo@pg.edu.pl, alistani@pg.edu.pl

[2] Joint Institute of Machine Building, National Academy of Sciences of Belarus, ul. Akademicheskaya 12, Minsk, 220072 Belarus; al_kom@tut.by

[3] 81-572 Gdynia, Darmoki 13a/3 Poland; lukaszbolewski@gmail.com

* Correspondence: mszkodo@pg.edu.pl; Tel.: +48 666 055 620

Abstract: Two ceramic coatings have been applied on 5056 and 7075 aluminum alloy by microarc oxidation (MAO) technology. The mass losses, surface morphologies and the phase constituents of the MAO coatings before and after cavitation tests were examined by means of digital scales, scanning electron microscopy (SEM) and X-ray diffraction (XRD), respectively. In order to assess the impact of the mechanical properties of the surface layer on cavitation erosion resistance, hardness (H), reduced Young's modulus (E), surface elastic properties (W_{el}), surface toughness (K_{IC}), structure continuity and resistance to delamination and cohesion forces were determined using nanoindentation and scratch tests. The results indicate that there is a correlation between cavitation erosion resistance and hardness, H/E ratio and surface elasticity.

Keywords: aluminum alloys; micro-arc oxidation; cavitation erosion; mechanical properties

1. Introduction

Aluminum alloys are widely used in the construction of machinery and equipment because of their advantages. The main advantages include low density, good strength and good corrosion resistance in a humid environment. For these reasons, aluminum alloys are commonly used in the aviation industry [1-7], in the construction of high-speed vessels [8, 9] or in the automotive industry [10-14]. However, many elements of machines and devices made of aluminum alloys show low resistance to tribological wear and low resistance to cavitation erosion. These disadvantages of Al alloys limit their usage in many cases. In order to improve the tribological properties and cavitation erosion resistance of Al alloys, various protective coatings are being used [15-18]. One of the very promising methods for producing protective coatings is the micro arc oxidation (MAO). This method can be produced on Al alloys Al_2O_3 ceramic coatings which provide high hardness. It is known that the properties of protective coatings depend on their production parameters as well as the phase composition of the coating [16, 17, 19-21]. However, there is no general agreement as to which mechanical properties give the coating its best cavitation erosion resistance. For example, Jafarzadeh et al. [22] showed, that higher hardness does not translate into higher cavitation erosion resistance of thermally sprayed Al_2O_3 +TiO_2 coatings. According to them, discontinuities in the microstructure are more important, as far as the cavitation erosion resistance of the coatings they study is concerned, than the hardness of the coatings. In turn Zou et al. [23] studied Al-Si alloys produced by selective laser melting. According to them, the higher hardness of alloys obtained by changing production parameters, provided alloys with greater resistance to cavitation erosion. The literature also describes examples of the greater cavitation erosion resistance of materials that have higher surface elastic properties determined in the nanoindentation test. For example in [24], the authors report that the solution treatment slightly decreased the hardness of the high-nitrogen austenitic stainless steel but significantly increased its

elasticity, which increased its cavitation erosion resistance. The authors associate greater cavitation resistance of steels with higher elastic properties with greater ability of surface to adsorb energy generated by imploding bubbles. Whereas Cheng et al. [18] tested the cavitation resistance of MAO coatings made of aluminum alloy 2124. They reported that cavitation erosion resulted from the effects of brittle fracture of the MAO coating. This conclusion shows that the greater resistance of the coating to brittle cracking expressed by a higher critical stress intensity factor should ensure its higher cavitation resistance. Another parameter found in the literature to describe the material's cavitation erosion resistance, either in bulk or in coating form, is the hardness/elasticity modulus (H/E) ratio. This ratio characterizes the resistance of the material to elastic deformation. However, it also appears that this parameter considered separately cannot be the basis for assessing the cavitation erosion resistance of materials. This statement is based on the report given in [18] that the cavitation erosion resistance of MAO coatings was in the reverse order to their H/E ratio. Because cavitation loads interact cyclically, there is also information in the literature about the relationship between cavitation erosion resistance and fatigue strength. Usually, higher fatigue resistance provides greater cavitation erosion resistance. However, the residual tensile stress introduced by MAO process can be the main factors of decreasing fatigue limits, and thus reduce the cavitation erosion resistance, because it accelerate the rate of crack growth [25].

From the reports cited above, it cannot be clearly stated what mechanical properties of MAO coatings will ensure their best resistance to cavitation erosion. The scientific objective of the study is to determine which mechanical properties of the MAO coating will ensure the highest cavitation erosion resistance. In order to determine the impact of mechanical properties on the cavitation resistance of two MAO coatings with different phase structure, the cavitation test, nanoindentation test, scratch test and microscopic investigation were performed. In order to determine the state of residual stress and crystallite sizes, XRD images were analysed using the Williamson Hall method. This work contributes to understanding the reasons for high cavitation erosion resistance of MAO coatings and it provides essential results on the overall potential of MAO coatings as a future solution for elements of machines and devices exposed to cavitation loads.

2. Materials and Methods

2.1. Substrate material

Two types of aluminum sheet, i.e. 5056 and 7075, were used for the tests. Table 1 shows the chemical composition of aluminum alloys used for specimen preparation. Four cylindrical specimens (two from 5056 and two from 7075 alloy) with a diameter of 20 mm and a height of 10 mm were cut from the sheets specimen with a spark erosion by wire electrical discharge machining (EDM) using AccuteX AU-300IA machine.

Table 1. Chemical composition of aluminum alloys used to produce MAO coatings.

Al alloy	Cu	Mg	Mn	Fe	Si	Zn	Ti	Cr	Al
5056	0.10	5.35	0.16	0.4	0.32	0.1	0.15	0.18	rest
7075	2.13	2.92	0.30	0.5	0.41	6.10	0.20	0.22	rest

Next, the specimen surfaces were grinded on 1500 grit sandpaper.

2.2. Micro arc oxidation

MAO coatings were applied onto one specimen of 5065 alloy and one of 7075 alloy. One specimen of 5056 and one of 7075 alloy was not covered with MAO coating and served as a reference specimen.

Before coating formation, the specimens were degreased with acetone and rinsed with distilled water.

The electrolyte was an aqueous solution of 2 g/L KOH and 5 g/L Na_2SiO_3. The electrolyte was agitated with compressed air. A forty liter stainless steel tub was used. The specimen acted as the anode and the tub wall acted as the contrary electrode. The system was cooled by cold water pumped through double walls of the tub. The electrolyte temperature was controlled at 25−30 °C throughout the process. The MAO treatment was carried out using a pulsed AC power source. The current density, voltage, frequency, duty cycle, and duration time were 25 A/dm^2, 280 V, 50 Hz, 50% and 60 min, respectively. After the treatment, the specimens were rinsed in distilled water and dried in air and next the specimens were grinded on abrasive papers with grain gradation 360 up to 1500 and mechanically polished using diamond paste.

2.3. Cavitation erosion test

In order to simulate a controlled cavitation environment, tests were performed on the ultrasonic cavitation test rig to explore the ceramic coatings cavitation erosion resistance according to ASTM G32-10 tests method recommendations. The tests were made by vibratory cavitation apparatus Hielscher UP400s. The vibrations are amplified by the sonotrode fitted to the horn and formed as a λ/2 vibrator and transferred via its end face to the medium to be sonically irradiated. The UP400s device was equipped with the H14 sonotrode which provides maximum of 110 µm peak to peak amplitude in water. The two kinds of ceramic coatings and one 5056 aluminum alloy specimen were investigated in distilled water under the same cavitation intensity. Tested specimens were treated with cavitation in counter stand with ultrasonic apparatus (see. Fig. 1). The vibratory apparatus for all

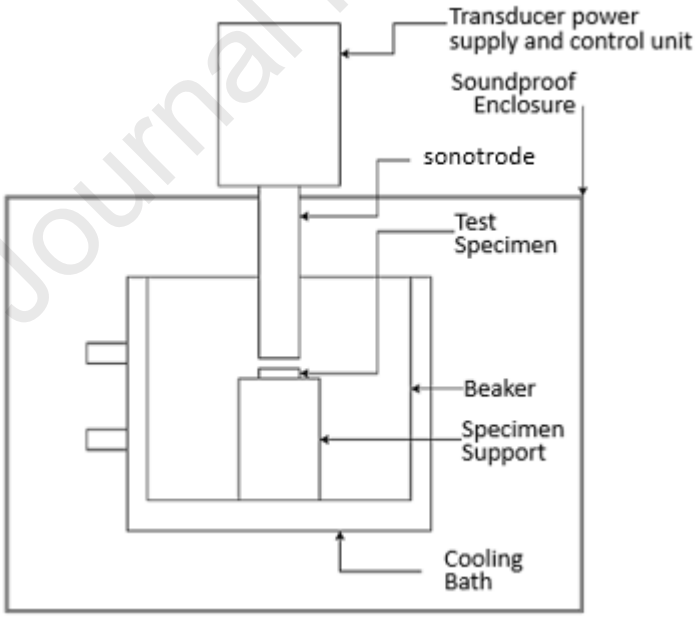

Fig. 1. Schematic drawing of cavitation stand for testing cavitation erosion resistance of MAO coatings.

tests was set to maintain amplitude of 50% which, for this configuration, stands for 0.05 mm peak to peak. The device maintained this amplitude by regulating output power. The average power needed was 45 Watts. The specimens were inserted into the counter stand at the distance of 0.5 millimeter from ultrasonic horn. The test was prepared in an environment of distilled water at constant temperature of 22 °C. After a fixed period of time specimens were removed, dried and weighed in. Mass loss was measured to 0.1 mg using a laboratory scales. Three samples from each MAO coating

and 5056 aluminum alloy were tested up to 13 h. The evaluation parameters of cavitation erosion resistance were the cumulative mass loss versus exposure time determined for each specimen, maximum erosion rate and length of incubation period. These values were determined as the arithmetic mean of three measurements.

2.4. Characterization

The microstructure and phase composition of the coatings before and after cavitation erosion test were examined with the aid of scanning electron microscope (SEM, JOEL JSM-7800F) equipped with X-ray energy dispersive spectroscopy (EDS), and light microscope (LM, Leica) respectively. A CT-scanner (phoenix v/tome/x s 240 kV) was used to measure the thickness of the MAO coatings. Computer Tomography (CT) parameters were as follows: voxel size 4.99 µm, voltage 80 kV, current 180 µA, detector type dxr-250 rt.

2.4.1. XRD analysis

The surface layer before and after cavitation erosion tests was examined with the aid of X-ray diffractometer (XRD, with Cu Kα radiation λ=0.15418 nm), operated at 30 kV and 50 mA. Bragg–Brentano focusing geometry was used to collect diffraction patterns over the 2θ range from 25° to 75° with a step size of 0.1° and counting time of 20 s per step. Instrumental broadening effects were evaluated and corrected using a silicon standard. The measured diffraction pattern was then fitted with the calculated Lorentz function using a nonlinear least-squares method in Origin software. Fig. 2 presents an example of line broadening analysis performed using the Lorentz function.

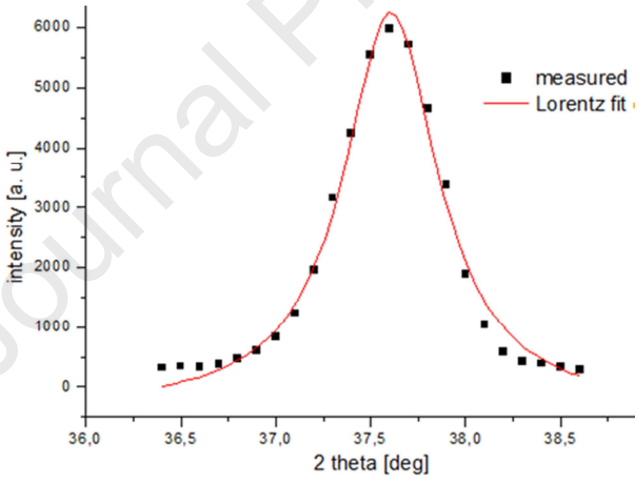

Fig. 2. A diffraction peak fitted with a Lorentz function for MAO coating

Williamson-Hall plot was used to estimate the size of crystallites and microstrain in the analysed surface areas. The Williamson Hall method assumes that the total peak broadening is the sum of the broadening resulting from the size of the crystallites and the presence of microstrain [26]:

$$B = \frac{a_S \cdot \lambda}{L \cdot cos\theta} + 4\varepsilon \frac{sin\theta}{cos\theta} \quad (1)$$

or,

$$B \cdot cos\theta = \frac{a_S \cdot \lambda}{L} + 4\varepsilon sin\theta \quad (2)$$

where: B is total broadening in radian, a_S is the Scherrer constant depends on the shape of the crystal, and the size distribution (here is assumed to be 1), λ is an electron beam wavelength 0.15405 in nm, L is crystallite size represents a crystal portion with exactly the same crystallographic orientation such as sub-grains in nm and ε is microstrain.

2.4.2. Nanoindentation test

Microhardness of the MAO coatings was measured with Nano Test Vantage nanoindenter using a Berkovich three-sided pyramidal diamond. The nanoindentation tests were performed with one load-unload cycle. Loading and unloading rate was 200 mN/s and 5s dwell at maximum load was applied. The maximum loads used in the nanoindentation tests ranged from 0.5 N to 4.3 N. Based on the load–displacement curves and applied Oliver and Pharr method, surface hardness (H), reduced Young's modulus (E) and surface elasticity were calculated as the arithmetic mean of ten measurements, using the integrated software. In the nanoindentation test, the elastic properties (W_{el}) of the surface were also determined as the share of the work of elastic deformation of the surface in relation to the total work done on deformation of the material. Figure 3 shows an example of two load-displacement curves obtained for MAO coating and 5056 aluminum alloy. The dashed area under the unloading curve represents the share of elastic deformation work (W_{el}), and the area under the load curve represents the total work of the deformation during the nanoindentation test.

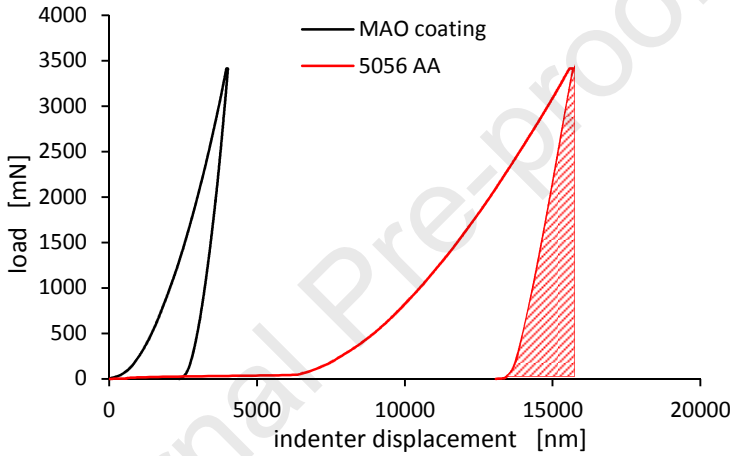

Fig. 3. Load vs. indenter displacement curves for BC coating and for 5056 aluminum alloy, obtained for the same maximum loads of 3.4 N.

In addition, surface toughness of MAO coatings was determined in the nanoindentation tests. In order to determine the surface toughness of the tested coatings, maximum loads of 12 N or 20 N were used. The indentation fracture (IF) method was used to calculate the fracture toughness of the MAO coatings. This method consists in relating the toughness of the material to the lengths of the cracks developing in the corners of the Berkovich indentation when a load (P) is applied. The method relies upon an optical measurement of the crack length. Cracks usually appear at the corners of the residual impression in brittle materials.

There are a number of equations that can be applied to calculate K_{Ic} by IF method. One of the most popular equations among the experimental group is the equation proposed by Dukino and Swain [27]. Knowing the Young's modulus and hardness, the fracture toughness K_{Ic} can be calculated using the formula:

$$K_{IC} = 1.073(0.015)\left(\frac{a}{l}\right)^{\frac{1}{2}}\left(\frac{E}{H}\right)^{2/3}\frac{P}{c^{3/2}} \quad (3)$$

where: E – Young modulus, H – hardness, P – maximum load during indentation, a, c, l – geometrical sizes presented in Fig. 4

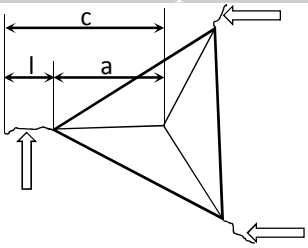

Fig. 4. A schematic indentation pattern from Berkovich indenter with radial cracks depicted by arrows [28]

Nanoindenter was also used for micro-scratch tests. The scratch test consisted of increasing the load applied to the diamond cone traveling on the surface along a 500 µm length. A cone that travels across the surface initiates various damages, that occur under different loads. Applying microscope observation, it is possible to determine the place of the occurrence of surface damage by means of geometrical relationships, critical loads causing their initiation. These critical loads were used to quantify the adhesive and cohesive properties of MAO coatings. In addition, failure points were determined through monitoring changes of frictional force and depth of scratch groove. During micro-scratch testing (MST) a conical diamond tip with 5 µm radius was drawn across the coated surface and raw alloy with an increasing load in the range from 0 to 1500 mN. The other scratch test parameters were as follows: scan velocity 3 µm/s and loading rate: 9 mN/s respectively.

3. Results

3.1. XRD and SEM analysis

As a result of the MAO process, Al_2O_3 coatings with different phase structure depending on the material of the substrate were obtained. Figure 5 shows the X-RD diffraction patterns for the coating obtained on a 7075 and 5056 aluminum alloy substrate. As it can be seen from Figure 5, the MAO coating produced on the 5056 aluminum alloy substrate is built entirely of a γ-Al_2O_3 phase. This coating is white, therefore it has been marked WC (white color). In turn, the coating produced on

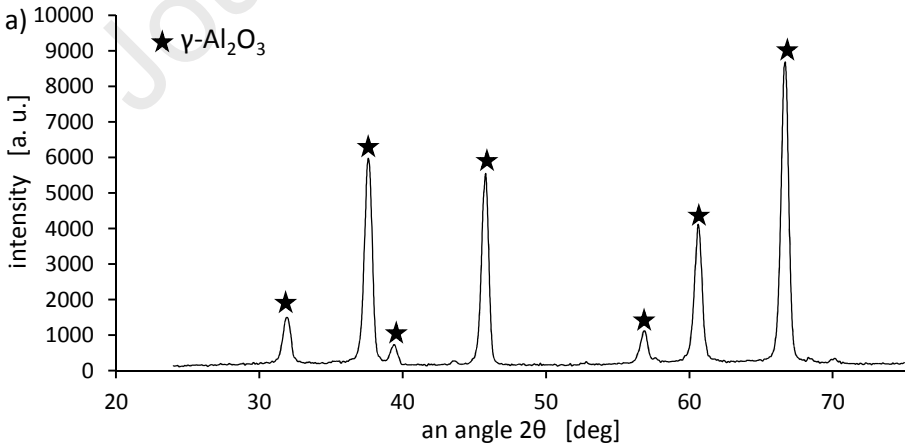

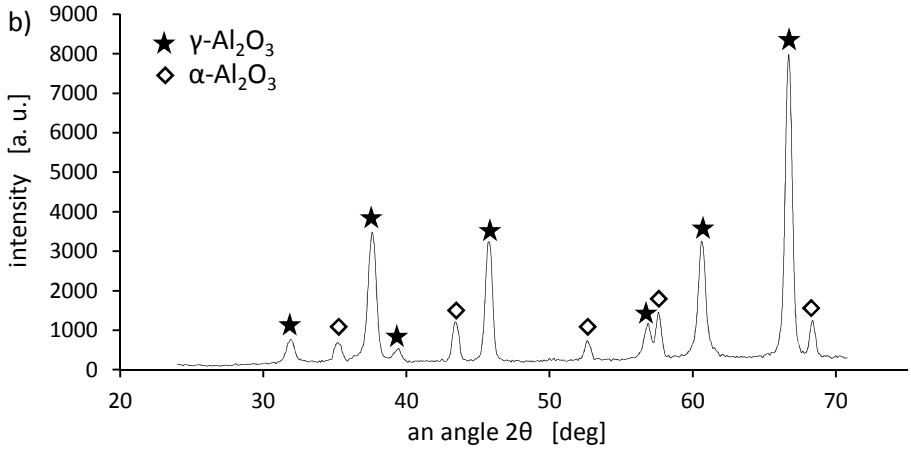

Fig. 5. XRD pattern of the (a) MAO coating on the 5056 aluminum alloy (WC) and (b) on the 7075 aluminum alloy (BC).

7075 aluminum alloy had a two-phase structure consisting of α-Al_2O_3 phase and γ-Al_2O_3 phase. The diffraction pattern analysis showed that the alpha phase in the coating structure was 19.7% and the gamma phase was 80.3%. This coating is black, therefore it has been marked BC (black color). Figure 6 shows a view of specimens for testing the cavitation erosion resistance of aluminum alloys with a white and black coating as well as specimens without MAO coating.

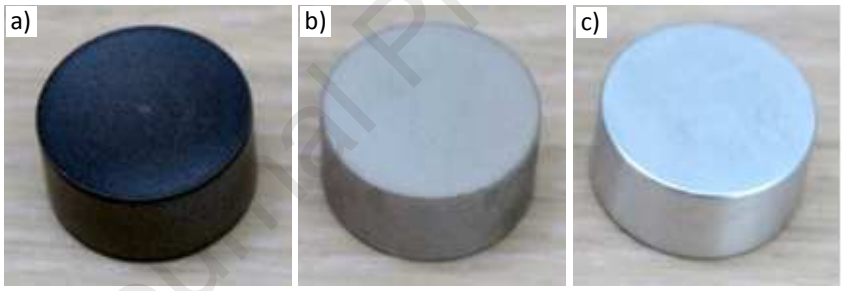

Fig. 6. Specimens of MAO coatings and aluminum alloy. (a) ("black coating" BC); (b) ("white coating" WC) and (c) aluminum alloy 5056.

Fig. 7 presents plots of Bcosθ vs. sinθ for α-Al_2O_3 phase and γ-Al_2O_3 phases being in WC and BC coatings. Table 2 summarizes the results of plots analysis and the minus indicates tensile stress. A modulus of elasticity used for calculating residual stress in α-Al_2O_3 and γ-Al_2O_3 phases were determined in nanoindentation tests, described in next section, using loads for BC coating 20 N and for WC coating 12 N, respectively. To determine the modulus of elasticity of both phases, it was assumed that the global modulus of elasticity is a weighted average for the gamma and alpha phases. In order to determine the thickness of the produced MAO coatings, scans were made using a computer tomography. Figure 8 shows a fragment of the CT scan made for the WC coating used to measure the thickness of the obtained coating. The tests carried out in this way showed that the average thickness of both MAO coatings obtained is the same and amounts to 130 μm.

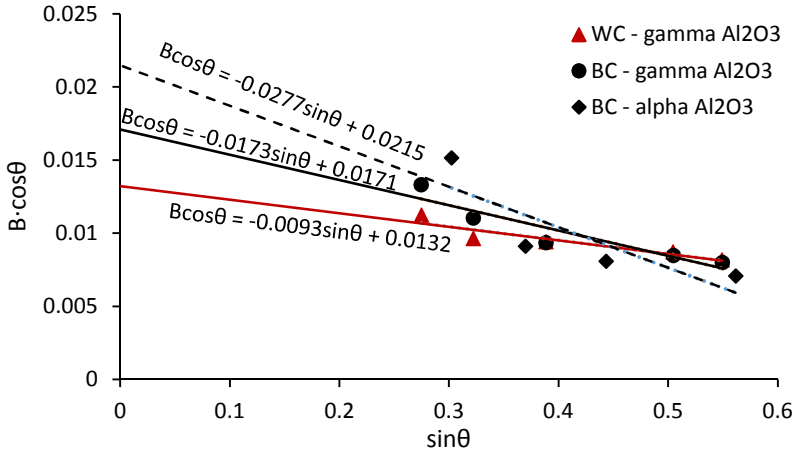

Fig. 7. Plots of Bcosθ vs. sinθ for γ-Al_2O_3 phase in BC and WC coatings and for α-Al_2O_3 phase in BC coating.

Table. 2. Microstrain, crystallite size and residual stress in WC and BC coatings

	λ (nm)	λ/L	L (nm)	4ε	ε	E (GPa)	σ_R (MPa)
WC γ-Al_2O_3	0.15418	0.0132	11.7	-0.0093	-0.00233	151.75	-354
BC γ-Al_2O_3	0.15418	0.0171	9	-0.0173	-0.00433	151.75	-657
BC α-Al_2O_3	0.15418	0.0215	7.2	-0.0277	-0.00693	110.84	-768

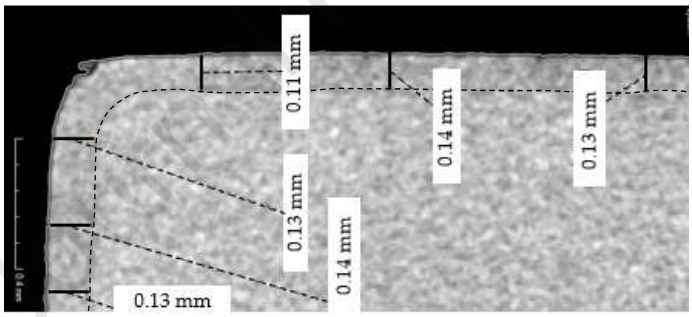

Fig. 8. Fragment of the CT scan for the WC coating with measured thickness.

3.2. Nanoindentation tests

In order to determine hardness, reduced Young's modulus and elastic properties of the obtained MAO coatings and 5056 Al alloy, a nanoindentation test was performed. Figures 9 and 10 show changes in hardness and reduced Young's modulus vs. contact depth of the indenter for MAO coatings obtained in the nanoindentation test for maximum loads varying from 0.5 N to 1.5 N. The measured hardness and modulus of elasticity of the surface layer differs depending on the maximum load applied to the Berkovich indenter. As it is shown in Figures 9 and 10, the indentation size effect (ISE) for both MAO coatings can be observed in indentation testing at different indenter displacements. This effect is not visible for 5056 aluminum alloy because at the same loads the indenter's displacement depth is much greater than in the case of MAO coatings and thus the impact of geometrically necessary dislocations is much smaller than for small indenter's displacement depths. Figure 9 indicates that the WC coating has a slightly higher local hardness than the BC coating, however, at higher loads and thus greater indenter depths, the global hardness of both

coatings is similar. In turn, Figure 10 shows the changes of the reduced Young's modulus for the tested MAO coatings depending on the contact depth of the indenter. Similar values for both coatings are also observed for the reduced Young's modulus.
The nanoindentation tests show that the elastic work W_{el} for the BC coating, WC coating and 5056 aluminum alloy was 44.5% ±1.6%, 39.6% ±1.9% and 25.7% ±1.1% respectively.

3.2.1. Surface toughness measurements

Figs. 11 and 12 present the view of dents after indentation testing for BC and WC coatings respectively, and Table 3 summarizes the data for calculations of fracture toughness of the MAO coatings. During the test, the WC coating showed cracks at the corners of the residual impression at 12 N load, while the BC coating at the same load did not crack. Therefore, for the BC coating, tests were carried out again for 20 N loads. According to the measurements, the BC coating has 38% less fracture toughness (4.82 MPa·$m^{1/2}$) than the WC coating (7.78 MPa·$m^{1/2}$).

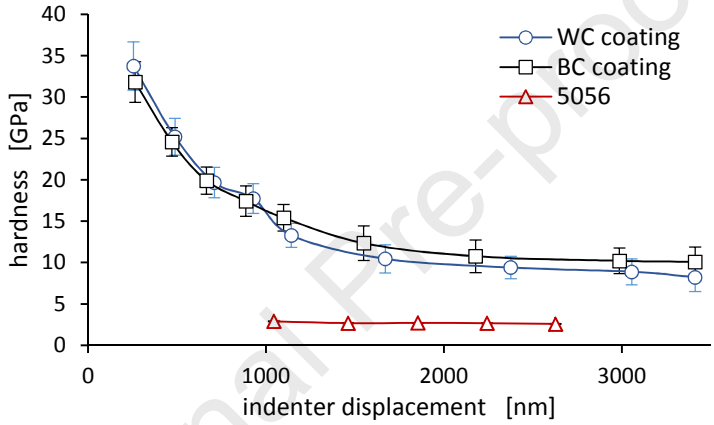

Fig. 9. Hardness vs. contact depth for both MAO coatings and 5056 AA. Error bars represent ± standard deviation of ten measurements.

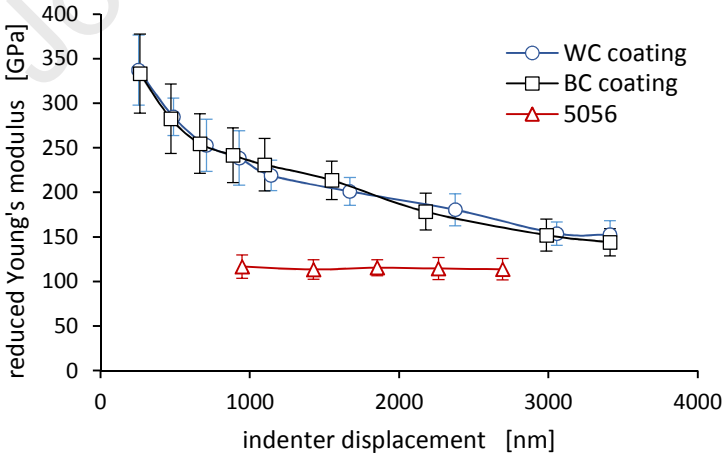

Fig. 10. Reduced Young's modulus vs. contact depth for both MAO coatings and 5056 AA. Error bars represent ± standard deviation of ten measurements.

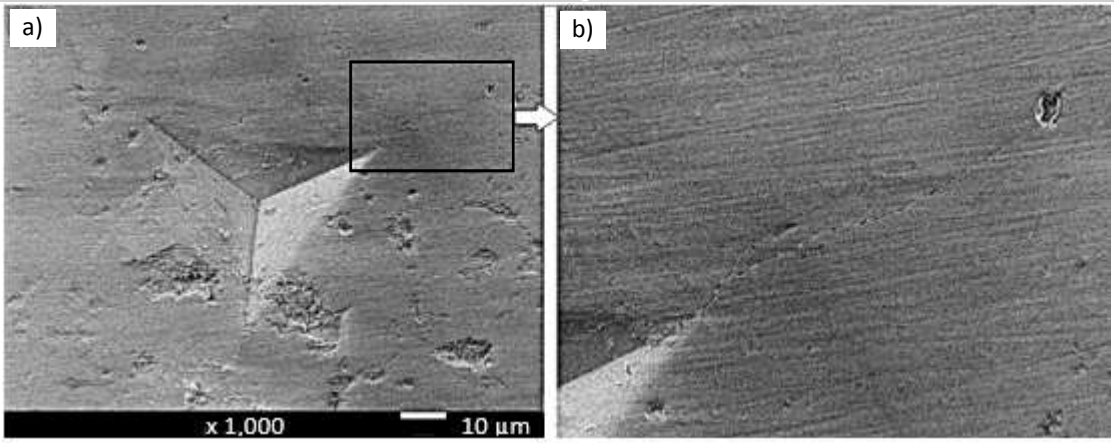

Figure 11. Dent view after nanoindentation testing for BC coating a) and an enlarged view of crack b).

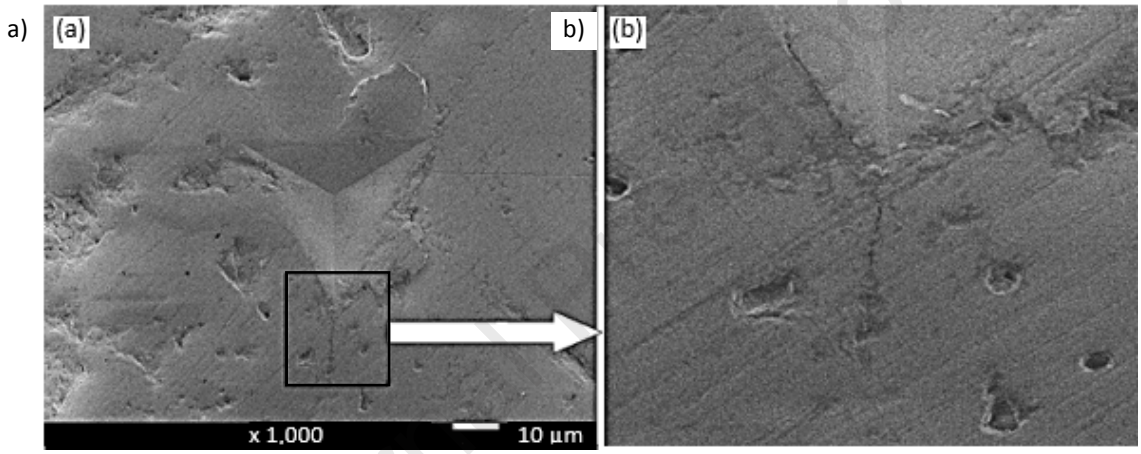

Fig. 12. Dent view after nanoindentation testing for WC coating a) and an enlarged view of crack b).

Table 3. Fracture toughness of the MAO coatings and data of their calculations.

coating	radius indentation (a) [µm]	crack length (l) [µm]	load (P) [N]	hardness (H) [GPa]	Young's modulus (E) [GPa]	toughness K_{IC} [MPa·m$^{1/2}$]
WC	23.64	13.64	12	8.25	151.75	7.78
BC	29.2	26.66	20	9.84	143.69	4.82

3.3. Scratch test

Figure 13 shows the surface images of MAO coatings and 5056 aluminum alloy after the scratch test. In the Fig. 13, white arrows indicate the places of occurrence of cracks developing in MAO coatings. In the case of BC coating, the detected crack developed parallel to the edge of the scratch groove and it initiated at a load of P_{cr} = 996 mN. In turn, for the WC coating, the crack occurred at a higher load of P_{cr} =1150 mN and it developed inside the scratch groove. In addition, material delamination occurred for this coating at a load of P_{del} = 1500 mN (depicted with a black arrow in Figure 13). However, in 5056 aluminum alloy, the scratch test did not cause cracks within the scratch groove. Plastic plowing was only observed for this material. Figure 14 shows the changes in scratch depth and friction coefficient recorded during the test. As it can be seen from Fig. 14a, changes in the friction coefficient as a function of increasing normal force applied to the diamond cone are in the range of

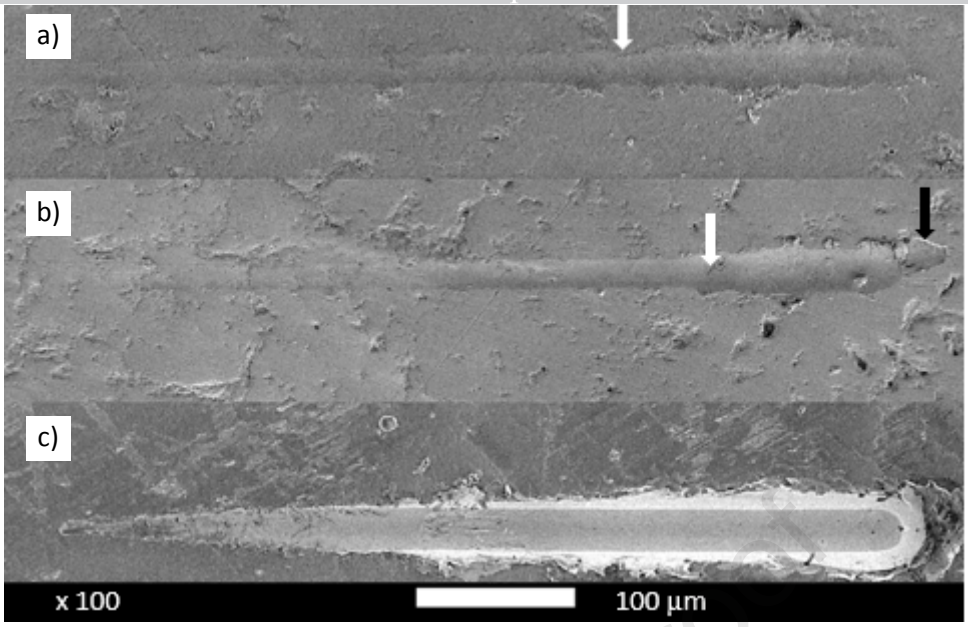

Fig. 13. View of the scratch on the BC coating surface a), on the WC coating b) and on the 5056 aluminium alloy **c**)

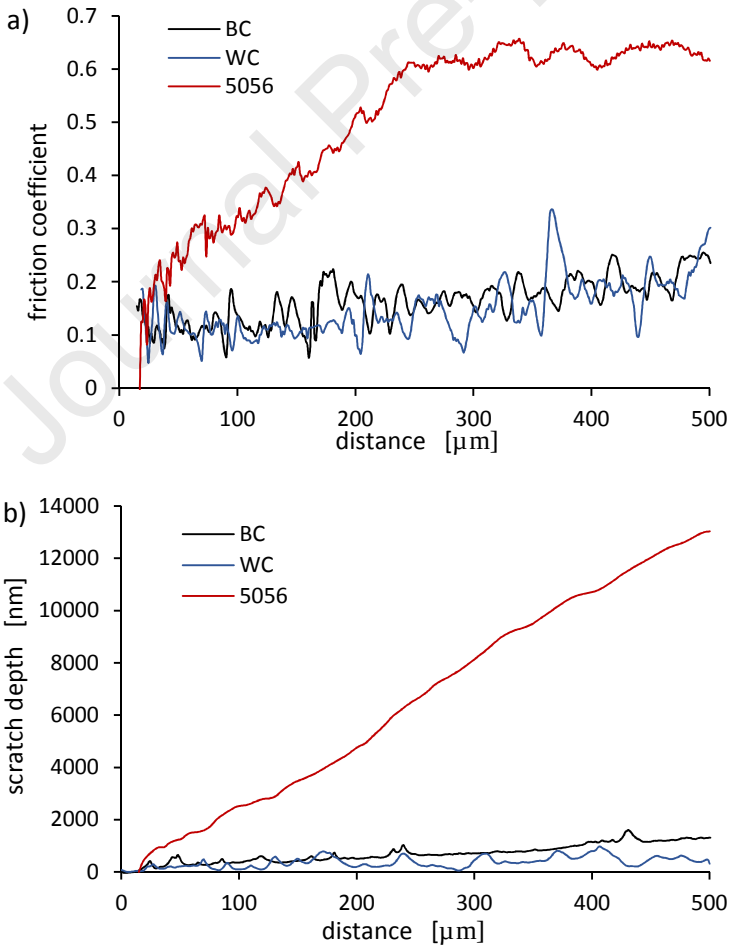

Fig. 14. Friction coefficient vs. distance traveled indenter a) and the depth of the grooves vs. distance b)

0.047 to 0.32 for WC coating and 0.057 to 0.24 for BC coating, respectively. For 5056 aluminum alloy, the change in the friction coefficient is range from 0 to 0.65. In turn, the greatest depth of the indenter penetration was shown in the 5056 aluminum alloy and the smallest one in MAO coatings. These results seem to be obvious from the point of view of the hardness of the MAO coatings compared to the hardness of Al alloys. The higher the global and local hardness of the coating is, the lower is the value of the indenter penetration.

3.4. Cavitation erosion test

In order to determine the cavitation erosion resistance of MAO coatings, cavitation tests were performed in which the cumulative mass loss (Δm) was recorded as a function of the time of cavitation loads. 5056 aluminium alloy was chosen as the reference material. Fig. 15 shows the course of erosion curves. For the determined cavitation erosion curves visible in Fig. 15 several characteristic periods of material destruction can be distinguished, i.e. the incubation period (τ_{inc}) for which there is no mass loss, the period of increasing cavitation erosion rate, the period of maximum cavitation erosion rate (MCER) and the period of decreasing erosion rate. Based on the data from the

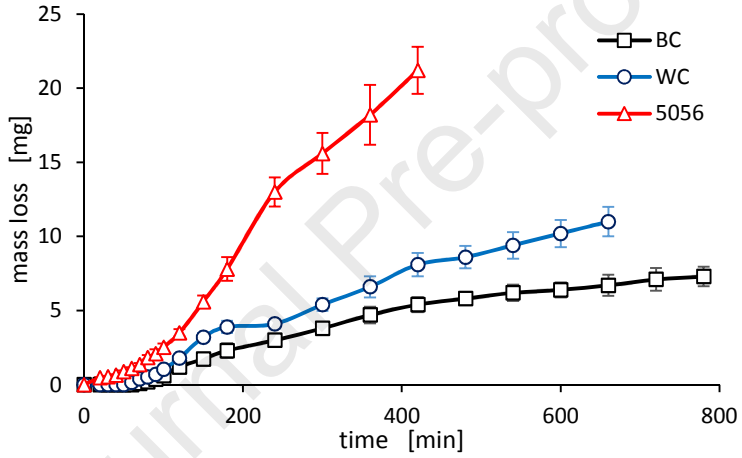

Fig. 15. Cumulative mass loss vs. cavitation load duration for MAO coatings and 5056 alloy. Error bars represent ± standard deviation of three measurements.

measurements of cumulated mass loss as a function of time Δm=f(t), the function d(Δm)/dt describing changes in the cavitation erosion rate in time was determined. Fig. 16 shows the changes in cavitation erosion rate over time. As it is shown in Fig. 16, the longest incubation period was recorded for the BC coating - 80 min and WC - coating 70 min, respectively. In turn, 5056 aluminum alloy did not show an incubation period. However, the highest cavitation erosion rate occurred for 5056 alloy - 0.087 mg/min, for WC coating it was 0.047 mg/min and BC coating it amounted to 0.031 mg/min. From the course of the d(Δm)/dt and Δm = f(t) curves it is also possible to determine the cumulative mass loss after 420 min (Δm_{420}) of the cavitation test, and the time to initiate the maximum erosion rate (τ_{MCER}) – see Fig. 16. Table 4 summarizes all values obtained on the basis of Figs 15 and 16. Table 4 also compares two indicators characterizing the cavitation erosion resistance (CER) of the tested materials, i.e. the reciprocal of the maximum cavitation erosion rate $(MCER)^{-1}$ and the R index calculated on the basis of the whole curves Δm=f(t) for a time interval of <0, 420 min>. The R index is the inverse of the area under the curve Δm=f(t), with the assumption that the area under the curve for the 5056 aluminum alloy is 1. The R index is therefore a dimensionless value relative to the reference material.

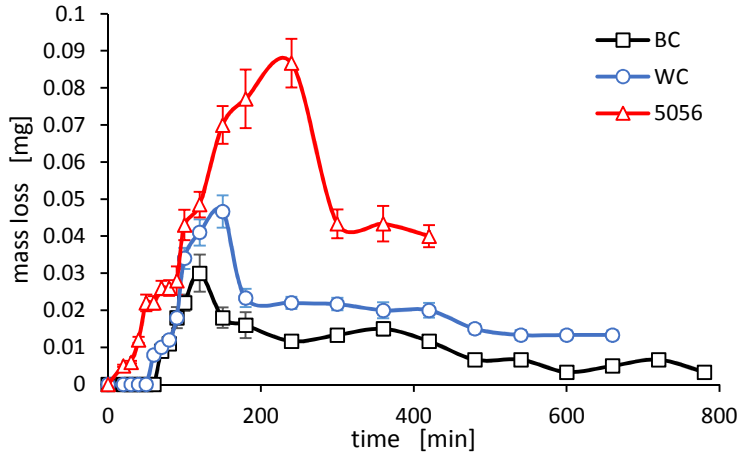

Fig. 16. Changes in cavitation erosion rate as a function of time for MAO coatings and 5056 alloy. Error bars represent ± standard deviation.

Table 4. Characteristic values obtained on the basis of cavitation erosion curves.

coating	τ_{inc} [min]	MCER [mg/min]	τ_{MCER} [min]	Δm_{420} [mg]	$(MCER)^{-1}$ [min/mg]	R [-]
WC	70	0.047	150	8.1	20	2.68
BC	80	0.031	120	5.5	32.25	3.98
5056	0	0.087	240	21	11.49	1

4. Discussion

Existing standards do not describe how to assess the cavitation erosion resistance of materials, nevertheless, many single-number parameters describing the material's cavitation erosion resistance can be found in the literature [29, 30]. One of the most common index of cavitation erosion resistance is the inverse of the maximum cavitation erosion rate $(MCER)^{-1}$. However, this indicator is based on only one value occurring for the erosion curve which is why the authors of this paper also decided to assess cavitation erosion resistance based on the entire cavitation erosion curve, i.e. based on the R index. It seems obvious that the mechanism of cavitation erosion of soft aluminum alloy and hard Al_2O_3 coatings is different. However, the authors of the publication decided to compare the impact of mechanical properties on cavitation resistance of investigated materials because various mathematical models describing the course of cavitation erosion can be found in the literature. The authors of these universal models use physical and mechanical properties of eroded materials to describe the course of cavitation erosion. Table 5 summarizes the cavitation erosion resistance and mechanical properties of the surfaces obtained in the nanoindentation and the scratch tests for MAO coatings and for 5056 aluminum alloy.

Table 5. Cavitation resistance of tested materials and mechanical properties of their surface

	R [-]	$(MCER)^{-1}$ [min/mg]	τ_{inc} [min]	τ_{MCER} [min]	Δm_{420} [mg]	H [GPa]	E [GPa]	K_{IC} [MPa·m$^{1/2}$]	P_{cr} [N]	P_{del} [N]	W_{el} [%]	σ_R [MPa]
WC	2.68	20	70	150	8.1	8.25	151.75	7.78	1.150	1.5	39.6	-354
BC	3.98	32.25	80	120	5.5	9.84	143.69	4.82	0.996	-	44.5	-679
5056	1	11.49	0	240	21	1.18	71	27*	-	-	25.7	-

*on the base [31] for similar 5083 aluminum alloy

On the basis of the data contained in Table 5, an analysis of the impact of the mechanical properties of the surface layer of the tested materials on their cavitation erosion resistance was made. As it was shown in Fig. 17, there is a monotonic correlation between cavitation erosion resistance, expressed both by $(MCER)^{-1}$ and R index, and global surface hardness. The increase in surface hardness increases the cavitation erosion resistance of materials. However, hardness cannot be the only effective parameter to determine the cavitation erosion resistance [22]. This parameter considered separately, without taking into account other mechanical properties of the surface, cannot be a measure of the cavitation erosion resistance of tested materials. The scratch test results showed that the smallest discontinuity of the microstructure, expressed by deviations from the trend curve for changes in the friction coefficient (see Fig. 14a), has been exhibited by 5056 alloy, which also has the lowest cavitation erosion resistance. However, when only comparing discontinuities for both MAO coatings, it can be seen that BC coating, with a smaller structure discontinuity, has a higher cavitation erosion resistance.

Another parameter that can be used to correlate mechanical properties with cavitation erosion resistance is H/E ratio. As it was shown in Fig. 17 b, the cavitation resistance of the tested materials

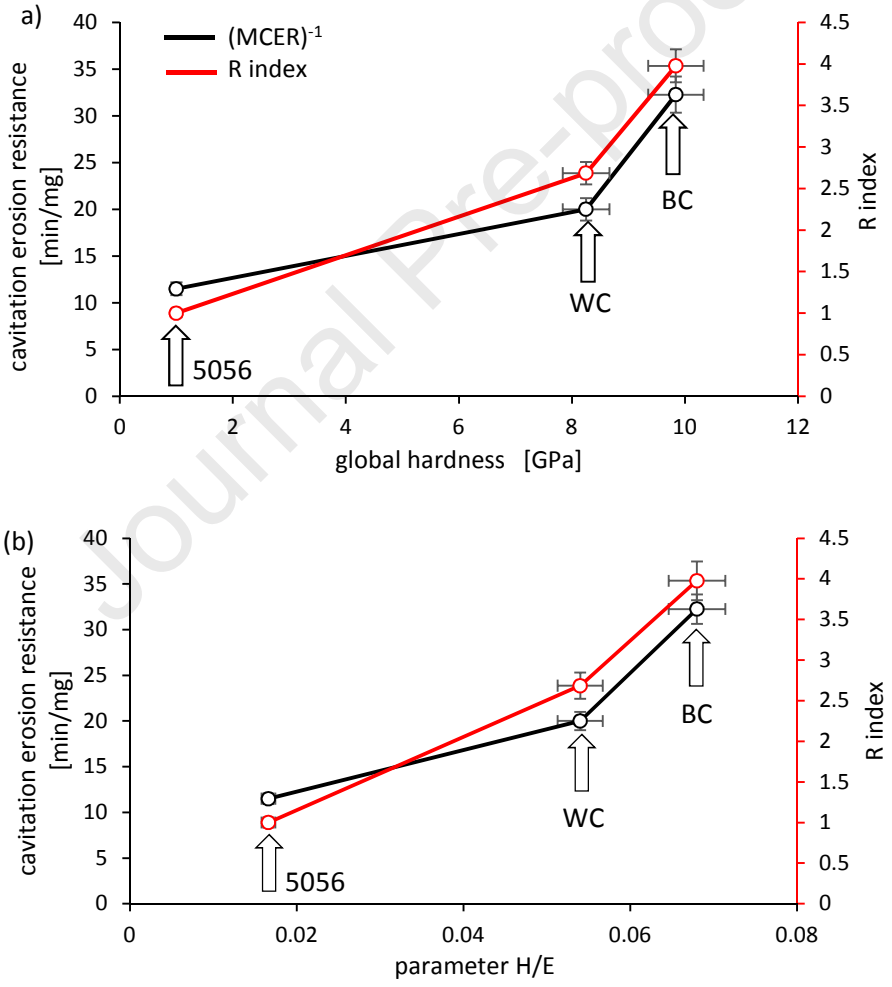

Fig. 17. Changes in cavitation erosion resistance depending on the global surface hardness (a) and depending on the H/E ratio (b). Error bars represent the ± standard deviation of the measurements.

increases with the increase of this ratio. The increase of the surface stiffness is accompanied by dissipation of higher water energy through elastic deformation instead of causing brittle fracture. On the contrary, when the H/E parameter decreases, the large pits could form easier and faster due to work hardening and formation of microcracks in the hardened surface layer, leading to a higher

cavitation wear. However, there is no consensus that this parameter is always well correlated with cavitation erosion resistance of MAO coatings [18]. It seems that elastic properties of the surface affects cavitation wear in a similar way as the H/E parameter. The higher the share of the work of elastic surface deformation in the total deformation of the material, the less energy from imploding bubbles will be used for material erosion. Fig. 18a shows that the greater work of the elastic

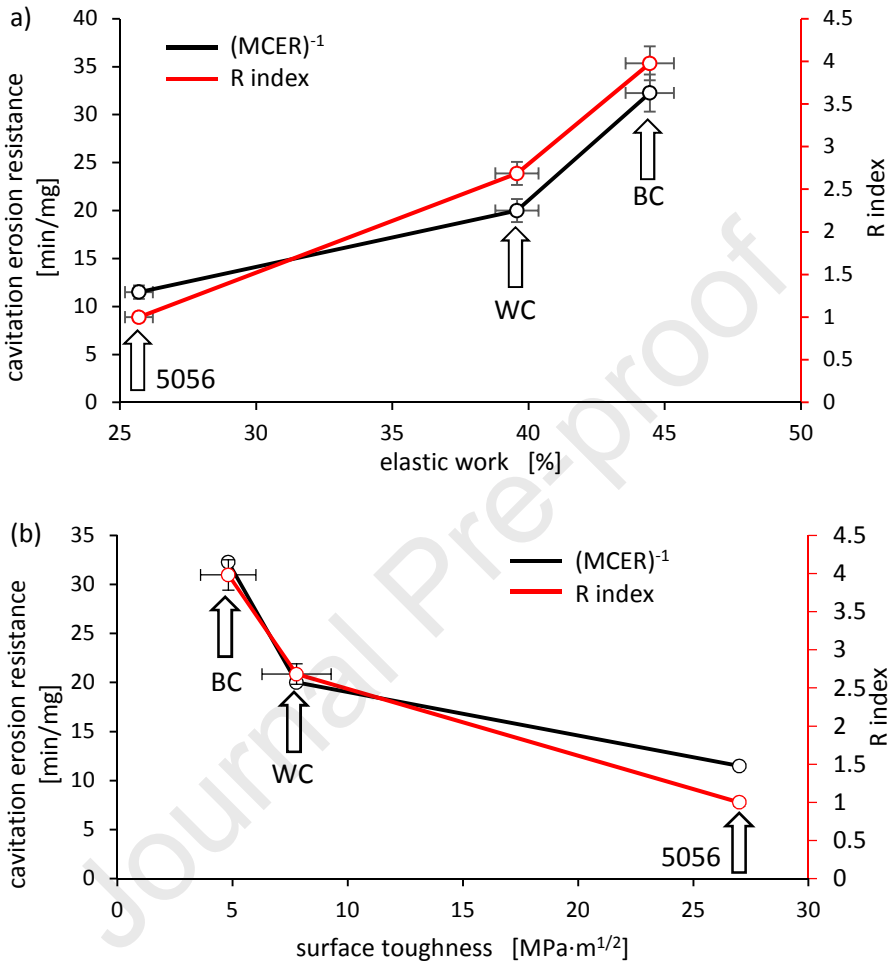

Fig. 18. Changes in cavitation erosion resistance depending on the elastic property of the eroded surface (a) and depending on the surface toughness of eroded surface (b). Error bars represent the ± standard deviation of the measurements.

deformation of the surface in the nanoindentation test was demonstrated by both MAO coatings in relation to 5056 alloy, which results in their greater resistance to cavitation wear. BC coating has the highest surface elasticity, which translates into its highest cavitation resistance. In addition, as shown in Fig. 19, greater surface elasticity extends the incubation period, which is beneficial from the point of view of the operation of flow machinery components exposed to cavitation damage. It also reduces the time after which the cavitation wear of material starts with the highest rate.
Surface toughness can be another property that increases cavitation erosion resistance. However, as shown in Figure 18b, the cavitation erosion resistance of the tested materials is in the reverse order to their fracture toughness. The BC coating with the lowest surface toughness shows the highest cavitation resistance and the 5056 alloy with the highest surface toughness has the lowest cavitation

resistance. In the case of the tested MAO coatings and the 5056 reference alloy, greater surface toughness caused later start of erosion at the highest rate (see Fig. 19). The scratch test also showed

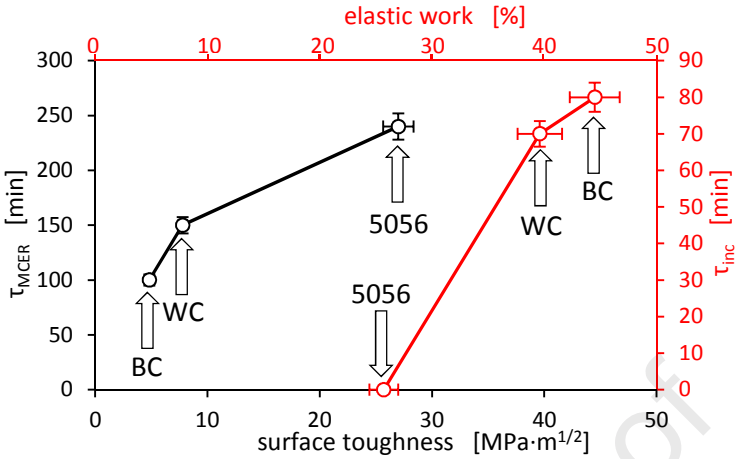

Fig. 19. The impact of surface toughness on the time when the material starts eroding at the highest rate and the relationship between the work of elastic deformation determined in the nanoindentation test and the incubation period. Error bars represent ± standard deviation of the measurements.

that in the case of the BC coating cracks occur at a lower critical load than in the case of the WC coating and, despite this, the BC coating showed greater cavitation resistance. Lower values of the normal force causing cracking of the MAO coating, as well as lower values of the critical stress intensity factor K_{IC} can be associated with residual stresses. Higher residual stresses in the BC coating than in the WC coating cause both lower values of the normal force causing cracking as well as lower K_{IC} values. Another reason for the lower fracture toughness of the BC coating can be the difference in its structure compared to the WC coating. Fig. 20 shows the micrographs of the structure of both coatings. As can be seen in Fig. 20a, there is a white mesh in the BC coating structure. Because the

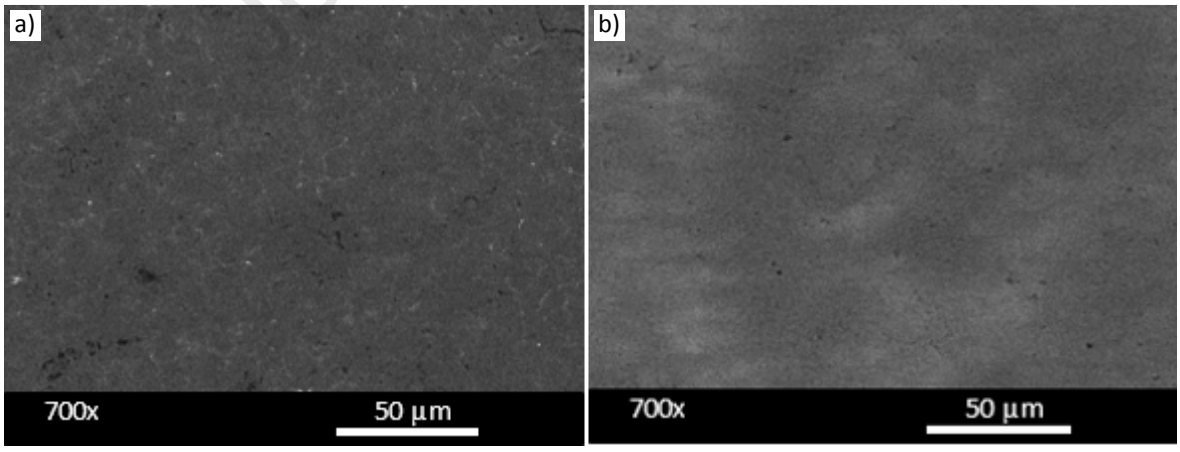

Fig. 20. Microstructure after micro arc oxidation process for the BC coating (a) and WC coating (b).

images were obtained with a BSE detector, it means the lighter areas of the image correspond to the elements with higher mass. Since the main alloying elements of the 7075 aluminum alloy with higher mass than Al are copper (2.13%) and zinc (6.1%), it can be expected that this mesh contains an increased concentration of these elements in the form of the oxides. Poisson's ratio of zinc and copper oxides is almost 2 times higher than that of aluminum oxide. Under mechanical load,

materials with lower Poisson's ratio have higher strain energy release rate than materials with higher Poisson's ratio. At the same time materials with a lower Poisson's ratio have a better resistance to thermally induced fracture [32]. Cavitation loads are both mechanical and thermal loads. Greater cavitation damage of WC coating, despite its greater surface toughness, can indicate a greater share of thermal loads in cavitation erosion than mechanical one.

It seems that the cavitation erosion resistance of MAO coatings strongly depends on their adhesion to the substrate and on the cohesion of the coating themselves. The erosion pits are caused by the violent implosions of the bubbles near the coating surface. For BC coating, the depth of penetration of cavitation loads was less than the thickness of the coating, due to its higher elasticity, and only some minor pits were formed on the surface of the coating as shown in Figs. 21a,b. For this coating, the size of cavitation pits ranged from 30 µm to 80 µm, and their distribution is presented in Fig 21c. In turn, for the WC coating, lower energy dissipation, caused by its lower surface elasticity, resulted in greater depth of penetration of cavitation loads and loss of coating adhesion to the substrate as shown in Fig. 21b. It seems that the distribution and size of pores occurring in the structure of the

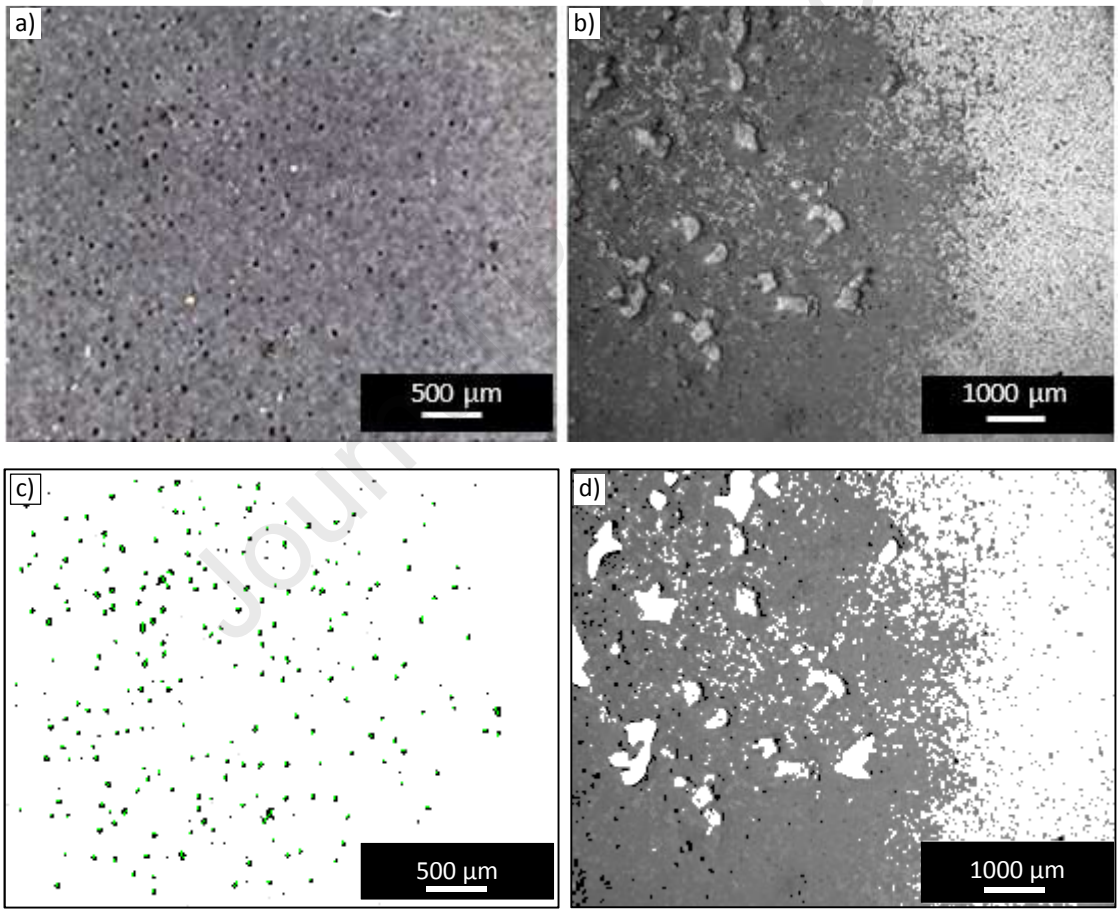

Fig. 21. View of the eroded BC coating surface (a) and the WC coating surface after the cavitation test (b). Binarized image showing the size and distribution of cavitation pits in the BC coating (c) and in the WC coating (d).

coatings, in addition to their phase composition, plays an important role in the course of cavitation destruction of MAO coatings. Pores, if they are not in close proximity, can similarly to the elasticity of the surface, partially absorb the energy of shock waves caused by bubble implosion and contribute to greater cavitation resistance. However, if they are large and occur in clusters, they will contribute to the reduction of cavitation resistance because, under the influence of cavitation loads, they will form

large cavitation pits. If the pores are too large, cavitation loads on their edge will cause a triaxial stress state to facilitate their enlargement and cavitation pitting. Fig. 22 shows the average pore size on the surface of both coatings after the micro arc oxidation process. SEM studies show that the pore size in the BC coating is smaller than in the WC coating. Undoubtedly, the microarc oxidation parameters affect the porosity of the coating. The relationship between the porosity of MAO coatings and the parameters of their preparation has been widely studied by many authors [33, 34]. In general, it can be noted that the strongest effect on the coatings porosity is exerted by the current density, the ratio of the anodic and cathodic current components, the duty cycle and the frequency of the forming voltage. For example, in the general case, as the current density increases, the porosity of the coating increases too. Therefore, knowing the basic relationships, it is possible to control the porosity of the coatings in the MAO process.

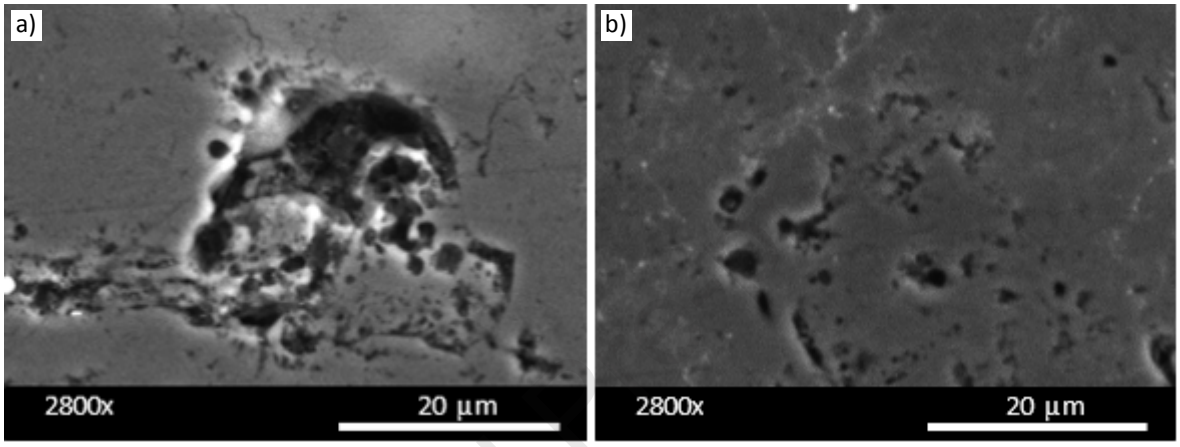

Fig. 22. View of the pores on the surface after micro arc oxidation process for the WC coating (a) and BC coating (b).

As shown above, the BC coating exhibited less structural discontinuity than the WC coating. This smaller discontinuity in the structure of BC coating results from a smaller number of pores than in the structure of WC coating. Occurring pores may also contribute to the delamination of MAO coatings. As the scratch test showed, the BC coating did not show any delamination while the WC coating at 1500 mN load was partially delaminated in front of the diamond cone face. Another reason for delamination during the scratch test could be the phase structure of the WC coating. Unlike the BC coating, the WC coating consisted completely of γ-Al_2O_3 phase, as shown by XRD studies. In turn, the BC coating consisted of 80.3% γ-Al_2O_3 and 19.7% α-Al_2O_3 phase. The schematic structure of the Al_2O_3 coating is shown in Fig. 23. MAO coatings, which have a hexagonal cellular

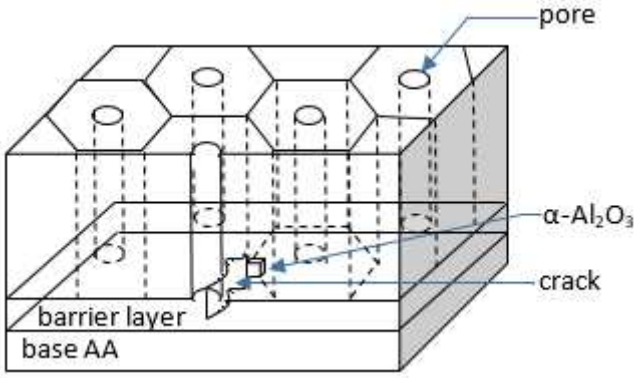

Fig. 23. Columnar and cellular structure of the Al_2O_3 coating.

structure, are most commonly described in the literature [35]. The cells have a columnar structure perpendicular to the substrate and in each column the pore runs through the entire thickness of the coating. The columns grow not directly on the aluminum alloy but on the barrier layer formed directly on the aluminum substrate. The thickness of the barrier layer is usually from 0.5% to 2% of the thickness of the entire Al_2O_3 coating. The pore diameter usually ranges from a dozen to several hundred nanometers. The presence of α-Al_2O_3 phase in the structure of the BC coating contributes to hinder the development of fatigue cracks in the barrier layer, from cyclically acting cavitation loads, which increases its adhesion to the substrate. Therefore, in the case of the BC coating, cavitation erosion proceeded by enlarging the primary pores. However, cavitation erosion mechanism for the WC coating was different. Due to lower adhesion of coating to the substrate, cavitation loads not only generated pitting enlargement at the primary pores but also caused fatigue cracking in the barrier layer and coating delamination as shown in Figs. 21b, d. The white areas in Fig. 21d show the exposed aluminum alloy substrate due to coating delamination.

In order to examine the impact of both phases on the cavitation erosion resistance, XRD tests were carried out once again after cavitation tests. Fig. 24 shows the XRD patterns for both MAO coatings.

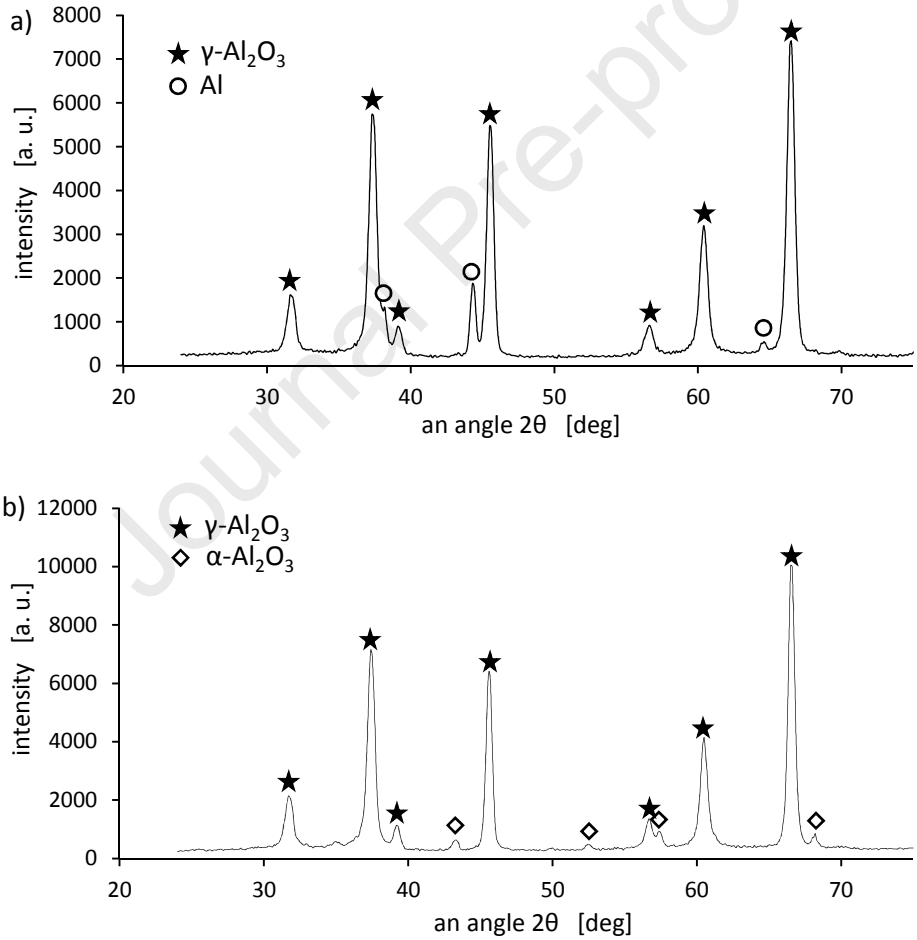

Fig. 24. XRD pattern of the (a) WC MAO coating after cavitation erosion test and (b) BC MAO coating after cavitation erosion test.

As a result of cavitation erosion in the structure of the BC coating, the share of α-Al_2O_3 phase decreased from 19.7% to 11.3%. However, this fact does not suggest that the presence of α-Al_2O_3 phase in the structure of MAO coating reduces cavitation erosion resistance, but it is just the opposite. Since the α-Al_2O_3 phase is more thermodynamically stable than the γ-Al_2O_3 phase, it is

unlikely that it will transform to the γ-Al_2O_3 phase under the cavitation loads. However, phase transformation in the other direction is possible, because during the collapse of cavitation bubbles at the center of implosion, the temperature can increase up to several thousand K [36]. After the cavitation test, for WC coating with the single γ-Al_2O_3 phase structure, the appearance of α-Al_2O_3 phase in the structure was not observed. However, for a BC coating with a two-phase structure, such a phase transition would be easier because such transformation occurs through nucleation and growth. The boundary of both phases can facilitate the nucleation of the α-Al_2O_3 phase. Thetransformation of γ-Al_2O_3 FCC phase (the specific density is 3.56 g·cm^{-3}) to α-Al_2O_3 hexagonal phase (the specific density is 3.98 g·cm^{-3}) is accompanied by a volume reduction of about 10% causing a large density increase [37, 38]. Such an increase in density, and at the same time a smaller volume loss of the eroded material, resulting from the fact that part of the energy from the imploding cavitation bubbles is consumed for phase transformation, may explain the smaller mass losses observed in the cavitation test for the BC coating. Also smaller sizes of γ-Al_2O_3 crystallites in the BC coating compared to the WC coating increase the number of obstacles that need to be overcome by dislocations and thus increase the stress caused by cavitation loads necessary to initiate cracks. Additional refinement of the structure in the BC coating is also provided by the α-Al_2O_3 phase, which has even finer crystallites than the γ-Al_2O_3 phase.

5. Conclusions

Two ceramic coatings have been applied onto the commercially available 5056 and 7075 aluminum alloy by microarc oxidation (MAO) technology. The coating made on the 5056 alloy had a single-phase γ-Al_2O_3 structure and the coating made on the 7075 alloy had a two-phase γ-Al_2O_3 + α-Al_2O_3 structure. Results of XRD pattern analysis, nanoindentation and scratch tests and cavitation erosion resistance of the obtained coatings and the reference alloy 5650 allow to draw the following conclusions:

1. There is a monotonic correlation between cavitation erosion resistance of investigated materials, expressed both by $(MCER)^{-1}$ and R index, and their hardness, H/E ratio and surface elasticity.
2. There is no correlation between cavitation erosion resistance and surface toughness. In this case, cavitation erosion resistance is in the reverse order of fracture toughness.
3. In the case of MAO coatings, their cavitation erosion resistance depends on the degree of microstructure continuity, expressed by a smaller variation of the friction coefficient in the scratch test.
4. The cavitation erosion resistance of MAO coatings depends more on their resistance to delamination under cavitation loads, and to a lesser extent on their resistance to cracking caused by collapsing bubbles.
5. A MAO coating with a two-phase structure has a higher cavitation erosion resistance than a coating with a single-phase structure despite higher residual stresses.
6. XRD studies indicate that under the cavitation load γ-Al_2O_3 → α-Al_2O_3 transformation is possible in a MAO coating with biphasic structure, which may contribute to an increase in the cavitation erosion resistance of the coating due to the fact that part of the energy from the imploding cavitation bubbles is consumed for phase transformation.

Author Contributions: Conceptualization, A.K. and M.S.; methodology, M.S and Ł.B.; validation, A.S.; formal analysis, M.S. and A.S.; investigation, Ł.B.; resources, M.S. and A.S.; writing—original draft preparation, M.S.; writing—review and editing, M.S.; visualization, A.S.; All authors have read and agreed to the published version of the manuscript.

Funding: The study was supported and conducted within the project Towards Intelligent Micro-Bearings – Tribological Aspects (ImBeing-FP7-.PEOPLE-2013-IRSES-612593) under the 7th European Community Framework Program (People, Marie Curie Actions).

Acknowledgments: The authors would like to thanks Grzegorz Gajowiec for SEM analysis, Mateusz Kmieć for conducting cavitation tests and Michał Antoszkiewicz for carrying out the nanoindentation and scratch tests.

Conflicts of Interest: The authors declare no conflict of interest. The funders had no role in the design of the study, in the collection, analyses, or interpretation of data, in the writing of the manuscript, and in the decision to publish the results.

References

[1] Y. Deng, R. Ye, G. Xu, J. Yang, Q. Pan, B. Peng, X. Cao, Y. Duan, Y. Wang, L. Lu, Z. Yin, Corrosion behaviour and mechanism of new aerospace Al–Zn–Mg alloy friction stir welded joints and the effects of secondary Al3ScxZr1−x nanoparticles, Corrosion Science 90 (2015) 359-374.
[2] Y. Deng, B. Peng, G. Xu, Q. Pan, Z. Yin, R. Ye, Y. Wang, L. Lu, Effects of Sc and Zr on mechanical property and microstructure of tungsten inert gas and friction stir welded aerospace high strength Al–Zn–Mg alloys, Materials Science and Engineering: A 639 (2015) 500-513.
[3] J. Goebel, T. Ghidini, A.J. Graham, Stress-corrosion cracking characterisation of the advanced aerospace Al–Li 2099-T86 alloy, Materials Science and Engineering: A 673 (2016) 16-23.
[4] M.M. Pariona, V. Teleginski, K.d. Santos, E.L.R. dos Santos, A.A.d.O.C. de Lima, R. Riva, AFM study of the effects of laser surface remelting on the morphology of Al–Fe aerospace alloys, Materials Characterization 74(0) (2012) 64-76.
[5] M.M. Pariona, V. Teleginski, K. dos Santos, A.A.O.C. de Lima, A.J. Zara, K.T. Micene, R. Riva, Influence of laser surface treated on the characterization and corrosion behavior of Al–Fe aerospace alloys, Applied Surface Science 276(0) (2013) 76-85.
[6] M.M. Pariona, V. Teleginski, K.d. Santos, S. Machado, A.J. Zara, N.K. Zurba, R. Riva, Yb-fiber laser beam effects on the surface modification of Al–Fe aerospace alloy obtaining weld filet structures, low fine porosity and corrosion resistance, Surface and Coatings Technology 206(8–9) (2012) 2293-2301.
[7] L. Xu, X. Yu, L. Hui, S. Zhou, Fatigue life prediction of aviation aluminium alloy based on quantitative pre-corrosion damage analysis, Transactions of Nonferrous Metals Society of China 27(6) (2017) 1353-1362.
[8] M. Orłowski, C. Bastien, O. Razmkhah, S. McCartan, Design methodology for crash occupant protection in cabin design of the high speed vessel, Marine Structures 51 (2017) 1-20.
[9] T. Magoga, S. Aksus, S. Cannon, R. Ojeda, G. Thomas, Identification of slam events experienced by a high-speed craft, Ocean Engineering 140 (2017) 309-321.
[10] Y. Boutar, S. Naïmi, S. Mezlini, L.F.M. da Silva, M. Ben Sik Ali, Characterization of aluminium one-component polyurethane adhesive joints as a function of bond thickness for the automotive industry: Fracture analysis and behavior, Engineering Fracture Mechanics 177 (2017) 45-60.
[11] F. Grosselle, G. Timelli, F. Bonollo, Doe applied to microstructural and mechanical properties of Al–Si–Cu–Mg casting alloys for automotive applications, Materials Science and Engineering: A 527(15) (2010) 3536-3545.
[12] J. Shin, T. Kim, D. Kim, D. Kim, K. Kim, Castability and mechanical properties of new 7xxx aluminum alloys for automotive chassis/body applications, Journal of Alloys and Compounds 698 (2017) 577-590.
[13] S.C. Ram, K. Chattopadhyay, I. Chakrabarty, High temperature tensile properties of centrifugally cast in-situ Al-Mg2Si functionally graded composites for automotive cylinder block liners, Journal of Alloys and Compounds 724 (2017) 84-97.

[14] B. Płonka, A. Kłyszewski, J. Senderski, M. Lech-Grega, Application of Al alloys, in the form of cast billet, as stock material for the die forging in automotive industry, Archives of Civil and Mechanical Engineering 8(2) (2008) 149-156.
[15] G. Hou, Y. An, X. Zhao, H. Zhou, J. Chen, S. Li, X. Liu, W. Deng, Improving interfacial, mechanical and tribological properties of alumina coatings on Al alloy by plasma arc heat-treatment of substrate, Applied Surface Science 411 (2017) 53-66.
[16] N. Xiang, R.-g. Song, J. Zhao, H. Li, C. Wang, Z.-x. Wang, Microstructure and mechanical properties of ceramic coatings formed on 6063 aluminium alloy by micro-arc oxidation, Transactions of Nonferrous Metals Society of China 25(10) (2015) 3323-3328.
[17] R. Kamal Jayaraj, S. Malarvizhi, V. Balasubramanian, Optimizing the micro-arc oxidation (MAO) parameters to attain coatings with minimum porosity and maximum hardness on the friction stir welded AA6061 aluminium alloy welds, Defence Technology 13(2) (2017) 111-117.
[18] F. Cheng, S. Jiang, J. Liang, Cavitation erosion resistance of microarc oxidation coating on aluminium alloy, Applied Surface Science 280 (2013) 287-296.
[19] Q.-P. Tran, Y.-C. Kuo, J.-K. Sun, J.-L. He, T.-S. Chin, High quality oxide-layers on Al-alloy by micro-arc oxidation using hybrid voltages, Surface and Coatings Technology 303, Part A (2016) 61-67.
[20] P. Wang, T. Wu, Y.T. Xiao, L. Zhang, J. Pu, W.J. Cao, X.M. Zhong, Characterization of micro-arc oxidation coatings on aluminum drillpipes at different current density, Vacuum 142 (2017) 21-28.
[21] P. Wang, T. Wu, Y.T. Xiao, J. Pu, X.Y. Guo, Effects of Ce(SO4)2 concentration on the properties of micro-arc oxidation coatings on ZL108 aluminum alloys, Materials Letters 182 (2016) 27-31.
[22] K. Jafarzadeh, Z. Valefi, B. Ghavidel, The effect of plasma spray parameters on the cavitation erosion of Al2O3–TiO2 coatings, Surface and Coatings Technology 205(7) (2010) 1850-1855.
[23] J. Zou, Y. Zhu, M. Pan, T. Xie, X. Chen, H. Yang, A study on cavitation erosion behavior of AlSi10Mg fabricated by selective laser melting (SLM), Wear 376-377 (2017) 496-506.
[24] Y. Qiao, J. Chen, H. Zhou, Y. Wang, Q. Song, H. Li, Z. Zheng, Effect of solution treatment on cavitation erosion behavior of high-nitrogen austenitic stainless steel, Wear 424-425 (2019) 70-77.
[25] K. Dejun, L. Hao, W. Jinchun, Effects of micro arc oxidation on fatigue limits and fracture morphologies of 7475 high strength aluminum alloy, Journal of Alloys and Compounds 650 (2015) 393-398.
[26] G.K. Williamson, W.H. Hall, X-ray line broadening from filed aluminium and wolfram, Acta Metallurgica 1(1) (1953) 22-31.
[27] R.D. Dukino, M.V. Swain, Comparative measurement of indentation fracture toughness with Berkovich and Vickers intender, Journal of American Ceramic Society 75(12) (1992) 3299-3304.
[28] M. Szkodo, A. Bień, M. Antoszkiewicz, Effect of plasma sprayed and laser re-melted Al2O3 coatings on hardness and wear properties of stainless steel, Ceramics International 42(9) (2016) 11275-11284.
[29] A. Szkodo, Mathematical description and evaluation of cavitation erosion resistance of materials, Journal of Materials Processing Technology 164 (2005) 1631-1636.
[30] M. Szkodo, Relationship between microstructure of laser alloyed C45 steel and its cavitation resistance, Journal of Materials Processing Technology 162 (2005) 410-415.
[31] R.J. Bucci, A.T. Center, G. Nordmark, J.E.A. Starke, Selecting Aluminum Alloys to Resist Failure by Fracture Mechanisms, ASM Handbook, University of Virginia, Department of Materials Science and Engineering, Virginia, 1996.
[32] J.E. Li, B.L. Wang, Effect of negative Poisson's ratio on the fracture mechanics parameters due to mechanical and thermal loads, International Journal of Engineering Science 150 (2020) 103256.
[33] R. Kamal Jayaraj, S. Malarvizhi, V. Balasubramanian, Optimizing the micro-arc oxidation (MAO) parameters to attain coatings with minimum porosity and maximum hardness on the friction stir welded AA6061 aluminium alloy welds, Defence Technology 13 (2017) 111-117.
[34] S-Y. Jian, J-L. Lee, H-B. Lee, H-H Sheu, M-H. Lin, Y-T. Shih, C-A. Chen, J-K. Chang, M-D. Ger, Correlation between Electric Parameters and Microstructural Properties of LZ91 Mg Alloy Coated by Micro Arc Oxidation. Int. J. Electrochem. Sci., 13 (2018) 5709 – 5722.

[35] H. Asoh, S. Ono, T. Hirose, M. Nakao, H. Masuda, Growth of anodic porous alumina with square cells, Electrochimica Acta 48(20) (2003) 3171-3174.
[36] E.B. Flint, K.S. Suslick, The temperature of cavitation, Science 253(5026) (1991) 1397-1399.
[37] Y. Yoshizawa, K. Hirao, S. Kanzaki, Fabrication of low cost fine-grained alumina powders by seeding for high performance sintered bodies, Journal of the European Ceramic Society 24(2) (2004) 325-330.
[38] S. Lamouri, M. Hamidouche, N. Bouaouadja, H. Belhouchet, V. Garnier, G. Fantozzi, J.F. Trelkat, Control of the γ-alumina to α-alumina phase transformation for an optimized alumina densification, Boletín de la Sociedad Española de Cerámica y Vidrio 56(2) (2017) 47-54.

Highlights

1. Two MAO coatings were made on 7075 and 5056 aluminum alloys
2. The MAO coating on 5056AA had a single phase γ-Al_2O_3 structure
3. The MAO coating on 7075AA had a biphasic α-Al_2O_3 + γ-Al_2O_3 structure
4. Cavitation tests were performed by using a ultrasonic cavitation test rig
5. Higher surface hardness and elasticity increase cavitation erosion resistance